Effects of Processing and Functionalization Methods on Nylon-6,6 Nanocomposites with Helical-Ribbon Carbon Nanofibers

I. Rodriguez-Pastor,[1] H. Varela-Rizo,[1] D. R. Bortz,[1] G. Montes de Oca,[2] I. Guinea,[3] I. Martin-Gullon[1]

[1]Department of Chemical Engineering, University of Alicante, Alicante, Spain
[2]CID, Centro de Investigación y Desarrollo Tecnológico, S.A. de C.V., Av. de los Sauces No. 87, Mz. 6, Parque Industrial Lerma, Lerma Edo. México, C.P. 52000, Mexico
[3]Grupo Antolín Ingeniería, Crta Irún 244, E-09007 Burgos, Spain

ABSTRACT: Helical-ribbon carbon nanofiber-based nylon-6,6 nanocomposites were obtained by three processing methods: *in situ* polymerization, solvent processing through coagulation, and melt compounding. Composites were produced with pristine carbon nanofibers and four functionalization treatments, HNO_3, O_3, air/NH_3, and ethylenediamine, which form sets of two liquid/gas phase treatments and two acidic/basic treatments. Dispersion was monitored at the microscale by optical microscopy, showing clear differences depending on processing and functionalization methods. The best dispersion was obtained by solvent processing, whereas the most appropriate functionalizations were obtained by air/NH_3 and ethylenediamine treatments. It was observed that lower aspect ratio CNFs and stronger CNF-matrix interaction increased crystallization temperature. Percolation was not detected in the melt-compounded composites while network formation was observed at concentrations of 2 wt % in the solvent and *in situ* processing methods, where a high-aspect ratio was critical for performance. © 2012 Wiley Periodicals, Inc. J Appl Polym Sci 000: 000–000, 2012

Key words: dispersions; crystallization; nanocomposites; carbon nanofiber; electrical properties

INTRODUCTION

Nylon-6,6, chemically known as polyamide-6,6 (PA66), is a semicrystalline thermoplastic polymer with a wide variety of applications. PA66 exhibits good chemical and abrasion resistance, has a low coefficient of friction, dimensional stability, toughness, and high stiffness and strength.[1,2] At the same time, carbon nanotubes and nanofibers (CNTs, CNFs) display superb thermal, electrical, and mechanical properties.[3,4] The potential fusion of these features has promoted significant interest in carbon-based nylon-6,6 nanocomposites for commercial use in the automotive and aeronautics industries.

Appropriate processing and achieving matrix-filler compatibility have proven crucial in obtaining well functioning nanocomposites.[5,6] Attractive van der Waals forces among nanofilaments together with the semicrystalline nature of nylon-6,6 often hinder adequate dispersion and produces agglomerated morphologies. Processing methods also affect dispersion of carbon nanofilaments in polymer matrices. Sahoo et al.,[2] achieved better multiwall carbon nanotube (MWCNT) dispersion in a PA matrix by extrusion and subsequent compression molding than extrusion plus injection molding. Furthermore, appropriate processing is important not only because influences dispersion but also because has an impact on material properties. Unfortunately, there is little literature comparing the effects of processing methods, especially for CNFs.

Chemical modification of nanofilament surfaces can promote filler-matrix affinity, thus improving dispersion and leading to greater mechanical performance.[7] PA66 nanocomposites containing pristine and aminofunctionalized MWCNTs produced by solution-casting were studied by Sengupta et al.,[8] The authors found agglomerates and nonuniform nanotube distribution in composites with pristine nanotubes. Aminofunctionalized MWCNTs appeared more homogeneously dispersed. Haggenmueller et al.,[9] made similar observations with PA66/SWCNT nanocomposites prepared by *in situ* polymerization. Amine groups on the nanotube's surface helped to achieve good dispersion in the polymer matrix but

pristine and HNO_3-treated nanotubes resulted in agglomeration.

Regarding electrical properties, percolation thresholds have been shown to depend on matrix disposition and nanofiber morphology.[10] Krause et al.,[11] working with melt-mixed PA66, determined that CNT production method and aspect ratio influenced percolation threshold. Haggenmueller et al.,[9] also observed that post-treated large aspect ratio CNTs led to higher electrical conductivity.

The degree of nylon-6,6 crystallinity and its interaction with CNTs are an often debated subject in the literature. Krause et al.,[10] reported crystallization temperature differences of 16°C between unprocessed neat PA66 and neat PA66 processed by melt-compounding. Linares et al.,[12] stated by DSC and WAXS that the presence of CNFs does not change crystallinity in PA66 nanocomposites. Additionally, functionalization may also have some influence on crystallinity.[8]

In this article, we report the effects of various processing and functionalization methods on PA66/CNF nanocomposites. The helical-ribbon CNFs utilized in this study are attractive for functionalization as they possess a unique orientation of the graphene layers with respect to the nanofiber's axis. Four surface treatments were carried out: Nitric acid (HNO_3) and ethylenediamine (EDA) liquid phase treatments and ozone (O_3) and air/ammonia (NH_3) gas phase treatments. Nanofibers were subsequently observed by transmission electron microscopy (TEM) and characterized by elemental analysis and quantitative chemical titrations. Nanocomposites were prepared by three methods: *In situ* polymerization, solvent processing, and melt-compounding. Fiber dispersion was subsequently observed by optical microscopy and analyzed by producing gray-scale histograms of the micrographs. Melting and crystallization temperatures and composite crystallinity were measured via differential scanning calorimetry (DSC). Surface electrical resistivity was measured by the two-point method.

EXPERIMENTAL

Materials

Helical-ribbon CNFs (GANF) were provided by Grupo Antolín Ingeniería (Burgos, Spain). These highly graphitic CNFs, with no presence of amorphous carbon coating, are synthesized by the floating catalyst method.[13] Structurally, they are formed by a continuous ribbon of 5–6 graphene layers that spiral helically about the nanofiber axis resulting as though the hollow nanofiber is formed by the stacking of truncated cones. This structure is responsible for high-electrical conductivity, provides a very reactive surface in comparison to CNTs and unique

toughening phenomena when dispersed in a polymer.[14]

PA66 in pellet form (Dinalon 66) was supplied by Grupo Repol (Spain) for melt-compounding and solvent processing. Adipoyl chloride (ADC) and hexamethylene diamine (HMD) were purchased from Sigma Aldrich for *in situ* polymerization.

CNF functionalization

Four surface treatments were applied to study the effect on PA66 nanocomposites, two in gas phase (O_3 and air/NH_3) and two in liquid phase (HNO_3 and EDA). Carboxylic functional groups were introduced to the CNF surface by HNO_3[15] (CNF-HNO_3) and O_3[16] (CNF-O_3) treatments. Nitrogen functional groups (amides and amines) were attached by NH_3[17] (CNF-NH_3) and EDA[18] treatments (CNF-EDA, obtained from CNF-HNO_3). Large-scale production of chemically altered nanofibers is more economically feasible in the gas phase. Moreover, liquid phase treatments involving nitric acid are known to excessively damage nanofiber morphology. These treatments were selected due to the probability of condensation between the functional groups introduced in CNFs and the amine and carboxylic terminal groups on the PA66 chain.

Nanocomposite preparation

Melt-compounded composites were prepared by combining the appropriate amount of CNFs and PA66 in the heated (270°C) chamber of a Haake Polylab laboratory mixer for 6 min. Higher temperatures and processing times result in matrix degradation. Compounding was performed with Banbury-type roller rotors at 60 rpm. This rotor speed offers the best nanofibers dispersion for the abovementioned processing conditions. Before mixing, PA66 pellets were dried at 90°C for 2 h. Nanocomposites with 1–10 wt % pristine CNFs and 1 wt % of each surface functionalized group were fabricated.

For solvent processing of the nanocomposites, PA66 was solved in formic acid while stirring to obtain a 10 wt % solution. A 1 wt % CNF/formic acid suspension was separately prepared with a high-shear rotor/stator laboratory mixer at 7000 rpm for 10 min. To stabilize the suspension by slightly increasing viscosity, a suitable amount of the 10 wt % PA66/formic acid solution was added to the CNF suspension to produce a CNF/PA66/formic acid solution at 3 wt % of PA66. Then, the mixture was poured into the remaining 10 wt % PA66/formic acid solution and mixed with the high-shear rotor/stator laboratory mixer (7000 rpm, 10 min). The resulting CNF/PA66/formic acid solution was then added to 700 mL of water. This method prevents
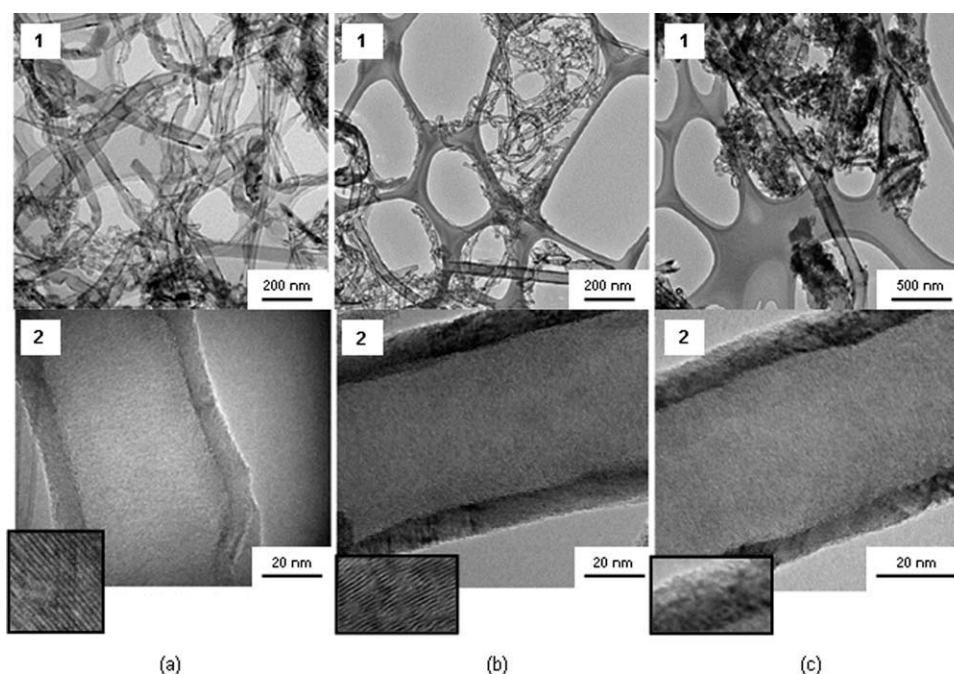
Figure 1 TEM images showing structure of (a1, a2) CNF-p, (b1, b2) CNF-O$_3$, and (c1, c2) CNF-EDA.

reagglomeration by quickly coagulating the polymer because of its insolubility in water. Solvent casting without coagulation step leads to the segregation of the nanofibers in the matrix at the macroscopic scale resulting in a worse dispersion. Finally, the nanocomposites were filtered to remove water and solvent, and dried under vacuum at 80°C for 24 h. Solvent-processed nanocomposites were prepared with both pristine (1–15 wt %) and functionalized CNFs (1–10 wt %).

In situ polymerization was carried out through an interfacial reaction of two immiscible phases, an organic phase (toluene) containing one of the monomers (ADC), and an aqueous suspension of CNFs containing the other monomer (HMDA). A 1 wt % CNF/water suspension was prepared with the rotor/stator laboratory mixer (7000 rpm, 10 min) and the appropriate amount of HMDA was subsequently added, together with sodium hydroxide to neutralize acidic byproducts during the reaction. Finally, both the water and organic phases were mixed and polymerization took place at the interface of the two immiscible phases. Resulting nanocompo-

sites were filtered, and later washed with water, acetone and toluene to remove the acidic reaction products that can degrade the composite. The collected material was dried under vacuum at 80°C for 24 h. Samples with 1–5 wt % pristine and 1 wt % functionalized CNFs were produced.

Films of each material having a thickness of 0.5 μm were obtained in a hot plate press at 265°C with a force of 2 metric tons for 2 min. Films were then manually cut into the required shapes for material characterization.

Characterization

Nanofiber morphology was observed by high-resolution TEM (JEOL JEM-2010). Surface functional groups were monitored by two methods. Elemental analysis (Carlo Erba CHNS-O EA1108) to establish C, H, N, and S content was performed on the dried CNF powders. Total acidic, carboxylic, and basic surface groups were determined by quantitative chemical titrations, according to the Boehm method.[19]

TABLE I
C, N, H, and O Content of CNFs Obtained by Elemental Analysis

Sample	C (%)	N (%)	H (%)	O (%)
CNF-p	96.19	0.09	0.27	2.06
CNF-HNO$_3$	93.80	0.30	0.25	5.65
CNF-O$_3$	90.52	0.47	0.37	7.16
CNF-NH$_3$	93.71	0.52	0.25	4.11
CNF-EDA	92.04	2.15	0.5	5.26

TABLE II
Acidic and Basic Surface Groups from Boehm Titrations

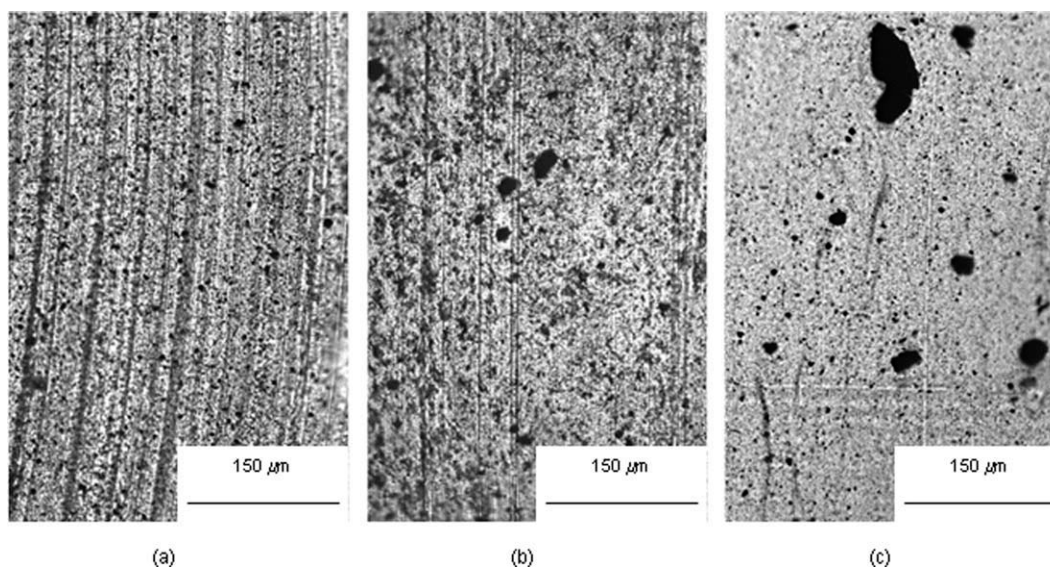| Sample	Total acidic groups (mmol/g)	Carboxylic groups (mmol/g)	Basic groups (mmol/g)
CNF-p	0.49	0.02	0.19
CNF-HNO$_3$	0.88	0.24	0.00
CNF-O$_3$	0.89	0.22	0.00
CNF-NH$_3$	0.48	0.00	0.25
CNF-EDA	0.84	0.00	0.69

Figure 2 Optical microscopy images showing dispersion of 1 wt % nanocomposites prepared with p-CNF by (a) solvent processing, (b) *in situ* polymerization, and (c) melt-compounding.
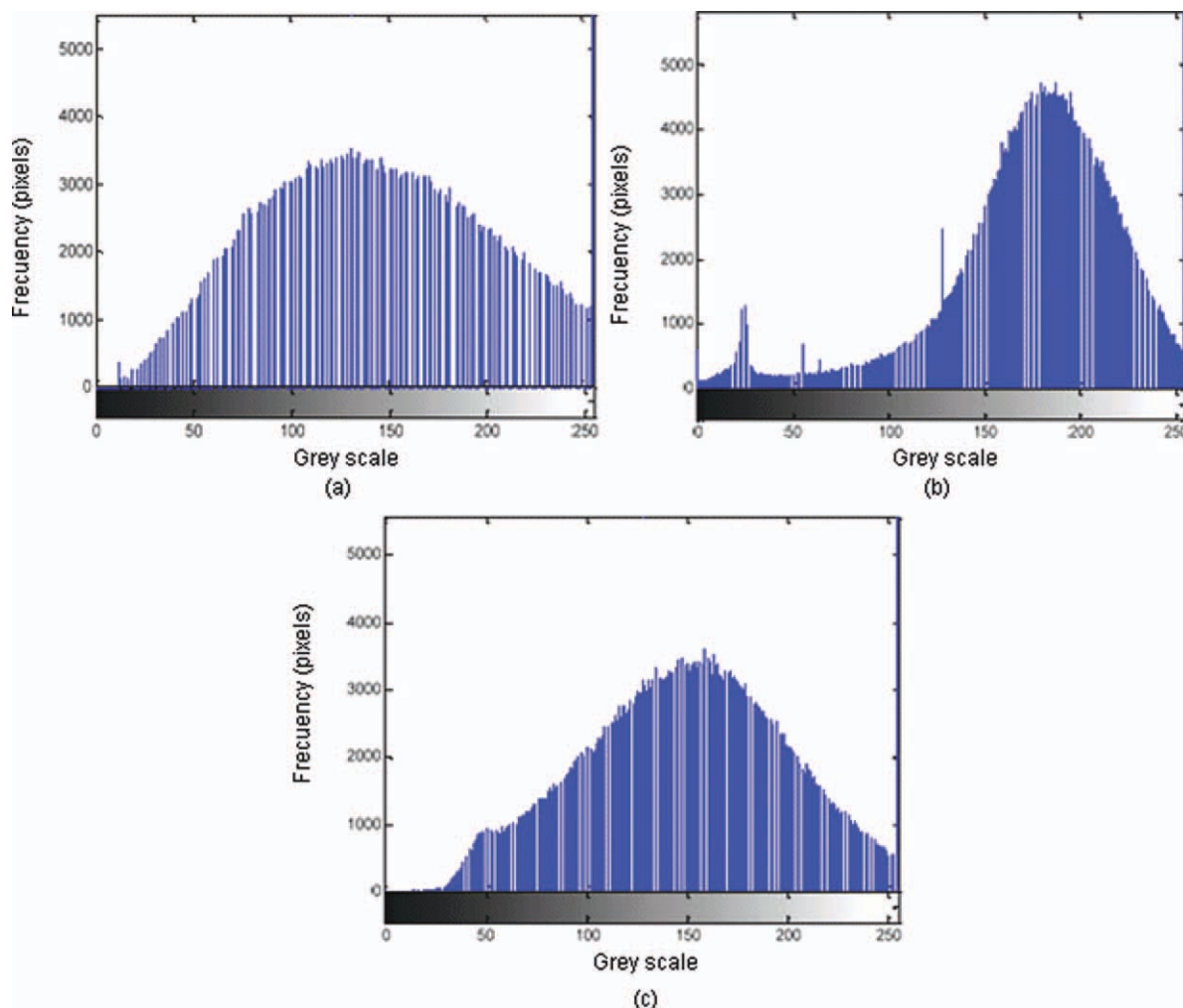

Figure 3 A total of 256 shade gray-scale histograms of 1 wt % nanocomposites obtained by (a) solvent processing, (b) *in situ* polymerization, and (c) melt-compounding. [Color figure can be viewed in the online issue, which is available at wileyonlinelibrary.com.]
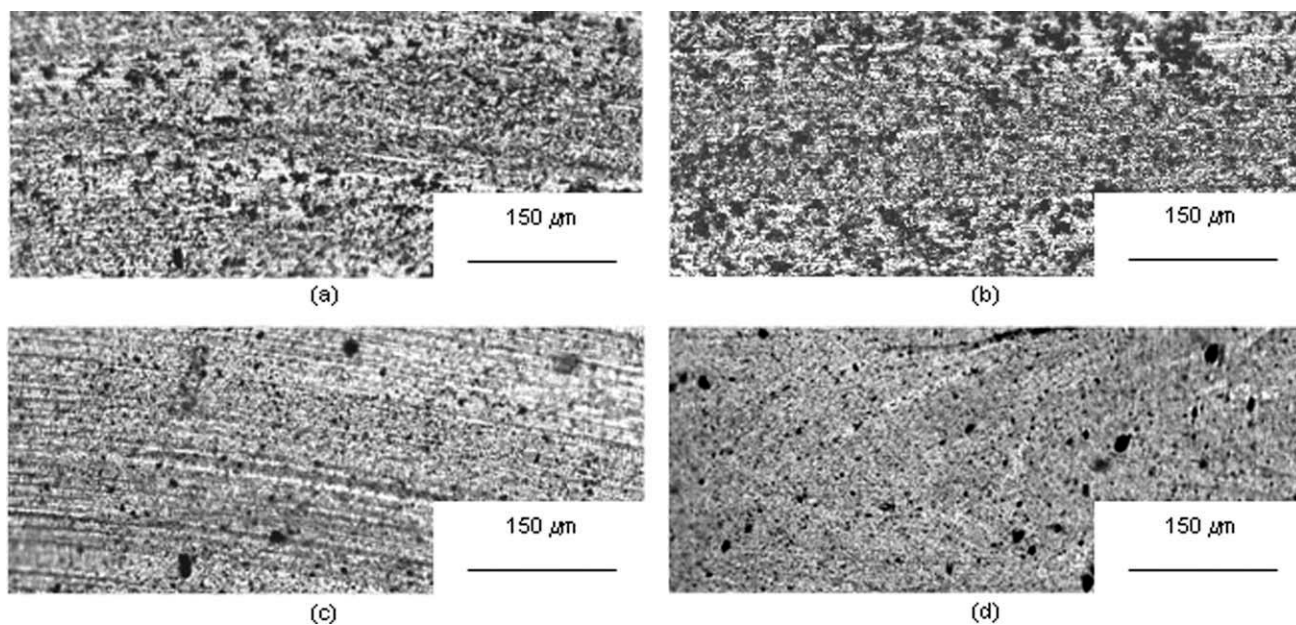
Figure 4 Optical microscopy images of 1 wt % nanocomposites prepared by solvent processing with (a) CNF-HNO$_3$, (b) CNF-O$_3$, (c) CNF-NH$_3$, and (d) CNF-EDA.

Microscale dispersion was evaluated by optical microscopy (Leica TCS SP2). Films having a thickness of 10 μm were cut with a microtome (RMC MTXL) and an area about 1.5 mm^2 was explored. To quantify the dispersion through the presence of agglomerates, these micrographs were analyzed using a 256 shade gray-scale histogram. Matlab R2006b software was used to numerically analyze the images using 256-grayscale values and to plot the histograms. A histogram with a normal distribution (symmetric and pronounced curve) indicates a good dispersion,[20] while a broad curve means that the dispersion is not homogeneous.[21] The presence of large agglomerates can results in a curve with two peaks whereas a shifted curve can indicate the absence of filler in some areas of the matrix.

Crystallinity of the CNF/PA66 composites was measured by DSC (TA Instruments Q100). Two consecutive heating scans were carried out from 25 to 300°C; the first was to remove thermal history, measurements were taken from the second. Heating and cooling rates were 10°C/min. The degree of crystallinity (X_c) was calculated following[22]:

$$X_c(\%) = \frac{\Delta H_f}{(1 - w) \cdot \Delta H_f^0} \cdot 100 \qquad (1)$$

where ΔH_f is enthalpy of fusion, ΔH_f^0 is enthalpy of fusion of 100% crystalline PA66, 196 J/g,[23] and w is the CNF weight fraction in the composite.

Surface resistivity was measured between two silver electrodes painted on the composite films. Measurements were done with a Prostat PSI-870 resistance and resistivity indicator (up to 10^{12} Ω/sq) and a digital multimeter (up to 5×10^8 Ω/sq).

RESULTS

CNF functionalization

TEM images confirmed various structural changes to the functionalized CNFs with respect to pristine nanofibers (CNF-p). Gas-phase functionalization with O$_3$ was observed to preserve the integrity and aspect ratio of the pristine nanofibers [Fig. 1(a1,b1)]. The NH$_3$-treated sample (not shown) yielded similar integrity. The HNO$_3$ and subsequent EDA [Fig. 1(c1)]-treated CNFs exhibited severe nanofiber shortening and morphology changes.

Under high magnification, the crystallographic modification after functionalization is observed. Both treatments [Fig. 1(b2,c2)] caused a loss of graphitic crystallinity due to defects and the introduction of surface groups. The graphitic planes are more defined in pristine CNF than in CNF-O$_3$, where these planes are not totally straight. The most noticeable change corresponds to the loss of this graphitic structure in CNF-HNO$_3$.

Elemental analysis (Table I) verified that both oxygen and nitrogen groups were successfully introduced to the nanofiber structure through functionalization. As expected, an increase in oxygen was observed in the CNF-HNO$_3$ and CNF-O$_3$ samples with slightly higher values for the latter. Addition of nitrogen containing groups was also confirmed in both nitrogen functionalizations. The EDA treatment was more effective, increasing nitrogen content from
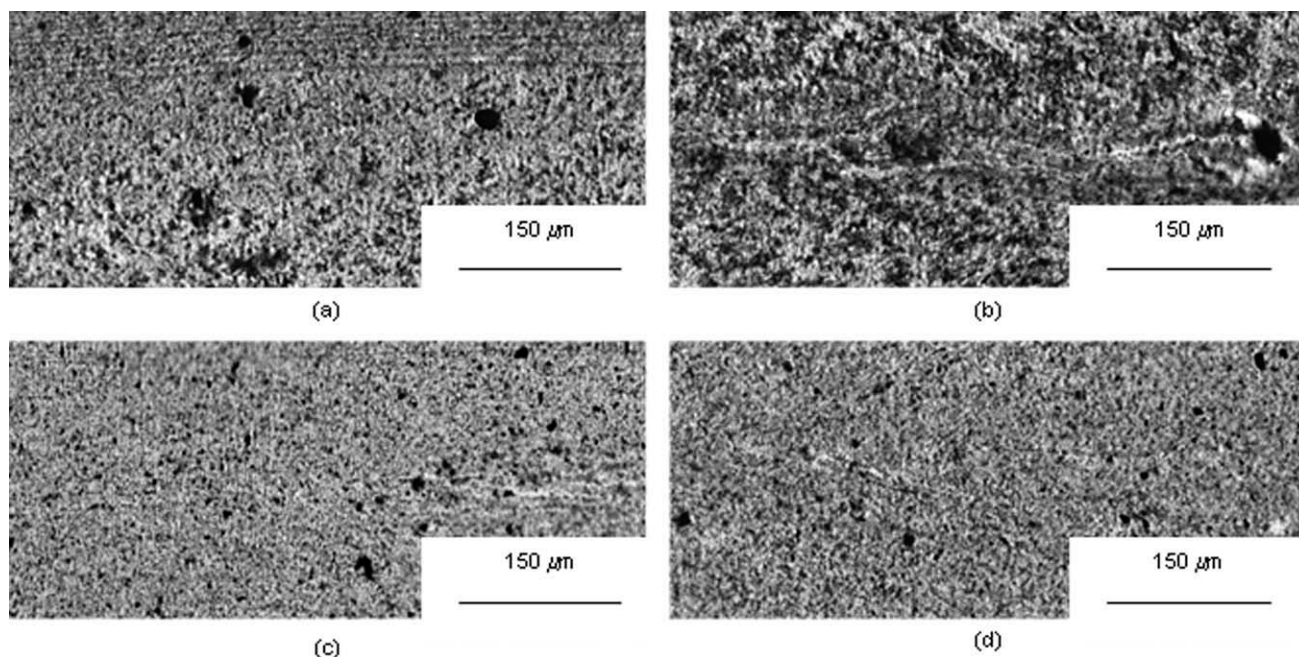
Figure 5 Optical microscopy images of 1 wt % nanocomposites obtained by *in situ* polymerization with (a) CNF-HNO$_3$, (b) CNF-O$_3$, (c) CNF-NH$_3$, and (d) CNF-EDA.

0.09% in the pristine CNFs to 2.15% in the CNF-EDA sample. As the CNF-EDA sample was previously treated with HNO$_3$, the increase in oxygen content must be considered since the oxygen containing carboxylic groups remain in the amide groups created through EDA treatment. Oxygen content was also observed to increase in the CNF-NH$_3$ sample owing to the fact that the treatment was conducted in an oxygen-containing atmosphere.

Titration results (Table II) show that total acidic group content was nearly doubled through the oxidative HNO$_3$ and O$_3$ treatments. A significant portion of the increase was determined to be the result of carboxylic groups that were successfully introduced to the nanofibers. An increase in basic groups, particularly in the CNF-EDA sample, corroborated the higher nitrogen content detected in the elemental analysis results.
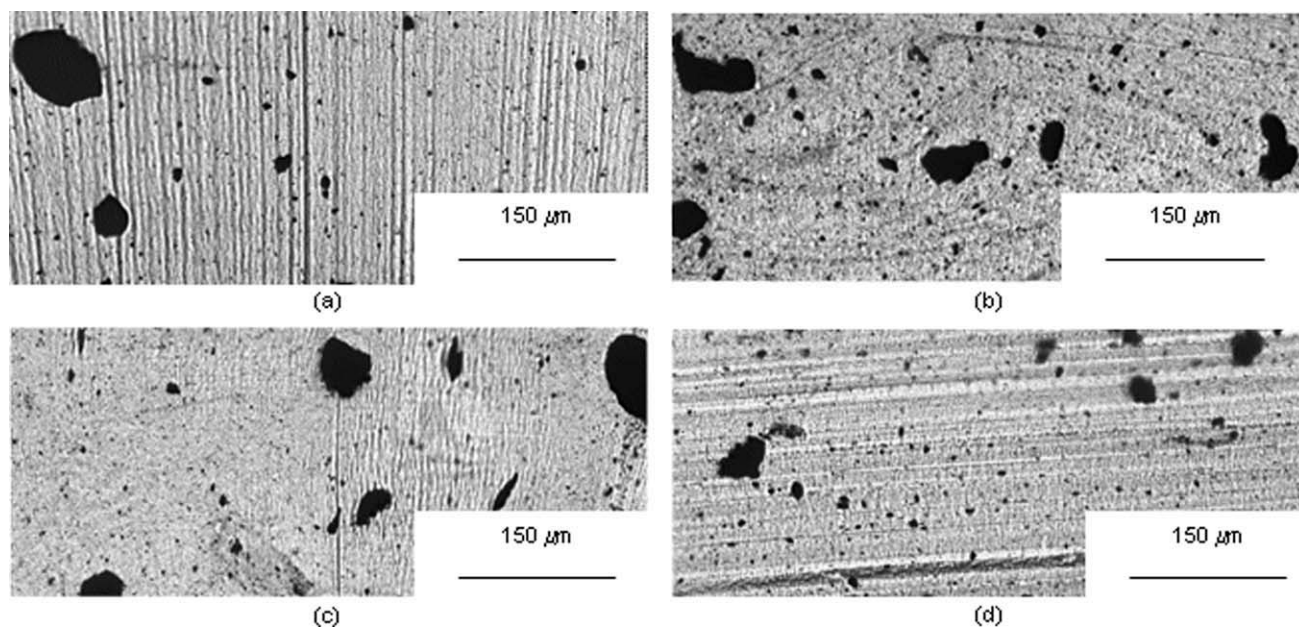

Figure 6 Optical microscopy images of 1 wt % nanocomposites processed by melt compounding with (a) CNF-HNO$_3$, (b) CNF-O$_3$, (c) CNF-NH$_3$, and (d) CNF-EDA.
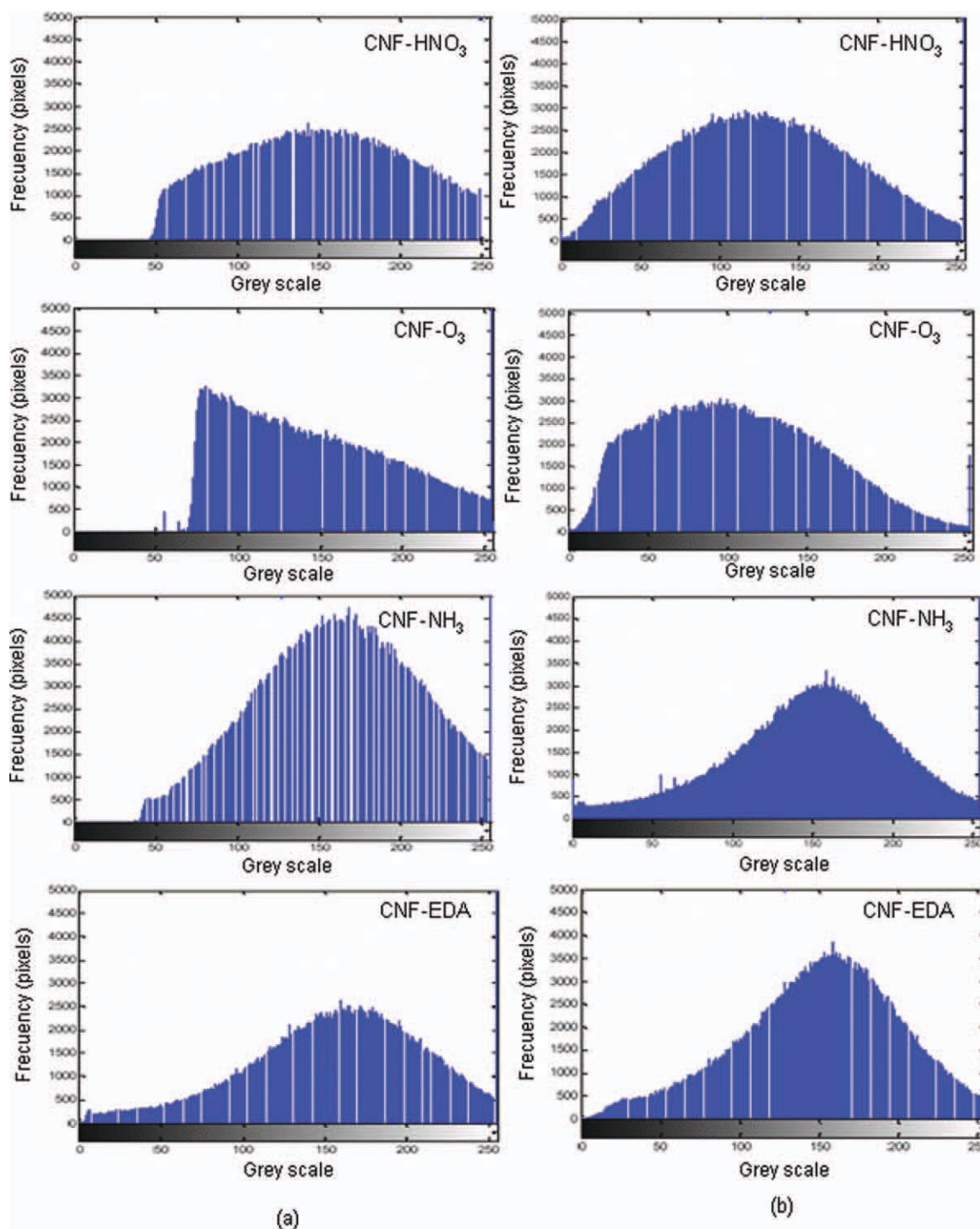
Figure 7 A total of 256 shade gray-scale histograms of 1 wt % nanocomposites with functionalized CNF obtained by (a) solvent processing and (b) *in situ* polymerization. [Color figure can be viewed in the online issue, which is available at wileyonlinelibrary.com.]

PA66/CNF nanocomposites

Dispersion

Figure 2 shows optical microscopy images of 1 wt % nanocomposites prepared by solvent processing, *in situ* polymerization, and melt-compounding. Large agglomerates, up to 50 μm, together with large

areas with few CNFs were detected in the melt-compounded sample [Fig. 2(c)]. On the other hand, no large agglomerates are observed in the solvent [Fig. 2(a)] and *in situ* [Fig. 2(b)] processed samples, suggesting these methods are more dispersive. The small agglomerates (5–10 μm) observed in the images may be due to CNF reagglomeration during
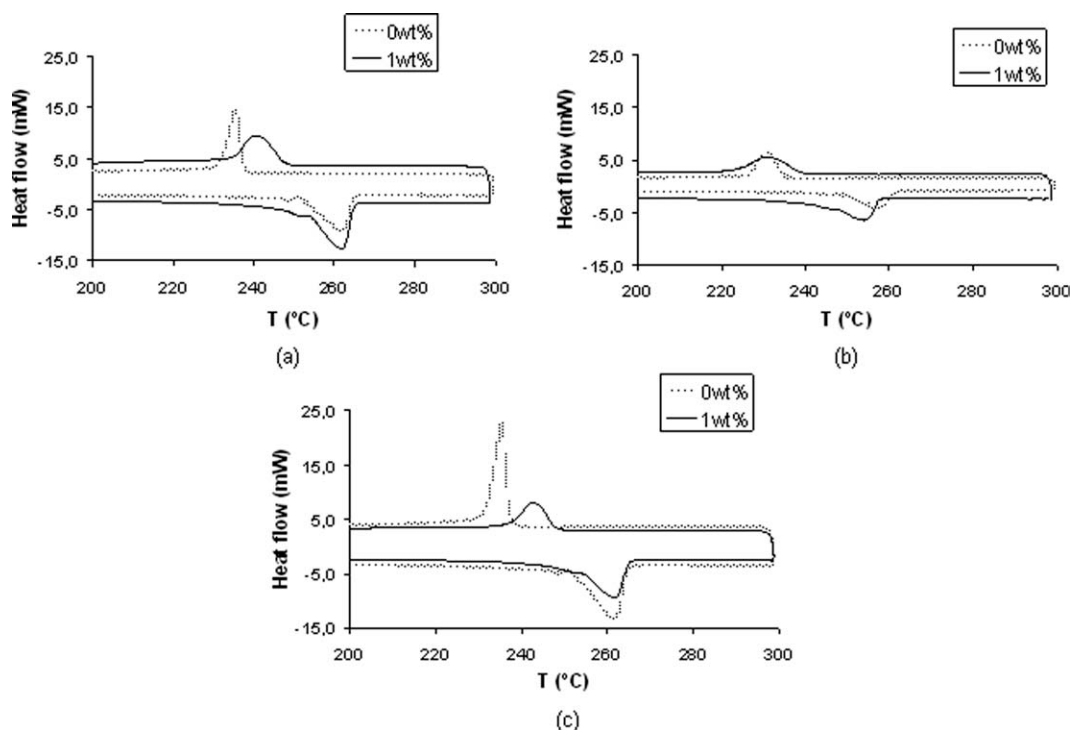
Figure 8 DSC thermograms for (a) solvent, (b) *in situ* polymerized, and (c) melt-compounded nanocomposites containing 1 wt % CNF-p.

crystallization. The solvent-processed composite appeared to have the most homogeneous distribution, containing the smallest and lowest occurrence of agglomerates.

Figure 3 shows the gray-scale histograms corresponding to micrographs in Figure 2. The melt-compounded distribution curve shows two peaks suggesting a sharp gradient in microscale dispersion. The larger of the two peaks is near the lighter side of the color histogram. This is a result of the composite containing areas with lower CNF concentrations than the bulk matrix. A sharp secondary peak appears on the dark side of the color scale due to the high level of agglomeration. This further indicates that the melt-compounded sample possesses a low-level dispersion. The solvent and *in situ* processed histograms contain peaks closer to the center of the distribution indicative of better CNF-matrix affinity and the absence of large agglomerates.[21] The *in situ* polymerization curve presents a slight shoulder on the left side of the distribution, albeit less pronounced than the secondary peak observed on the melt-compounded curve. Combined, the optical micrographs and the histograms point toward the solvent-processed samples as having the most appropriate distribution and dispersion of CNFs within the PA66 matrix.

In the composites containing surface functionalized nanofibers, both nitrogen treatments, CNF-NH$_3$ [Fig. 4(c)] and CNF-EDA [Fig. 4(d)], afforded better dispersions than the carboxylic containing samples, CNF-HNO$_3$ [Fig. 4(a)] and CNF-O$_3$ [Fig. 4(b)]. Sengupta et al.,[8] prepared PA66/MWCNT composites by solution casting and found more homogeneous dispersion with aminated nanotubes than pristine MWCNTs. Nanofibers containing carboxylic groups tend to form segregated networks. Similar segregation was observed by Xi et al.,[24] in polyethylene/MWCNT composites. The authors stated that the treated nanotubes could not migrate to crystalline regions of the matrix due to changes in their morphology and resulted in the filler being concentrated in the amorphous regions and gaps between crystals.

TABLE III
Crystallization Parameters for Neat PA66 and 1 wt % Nanocomposites

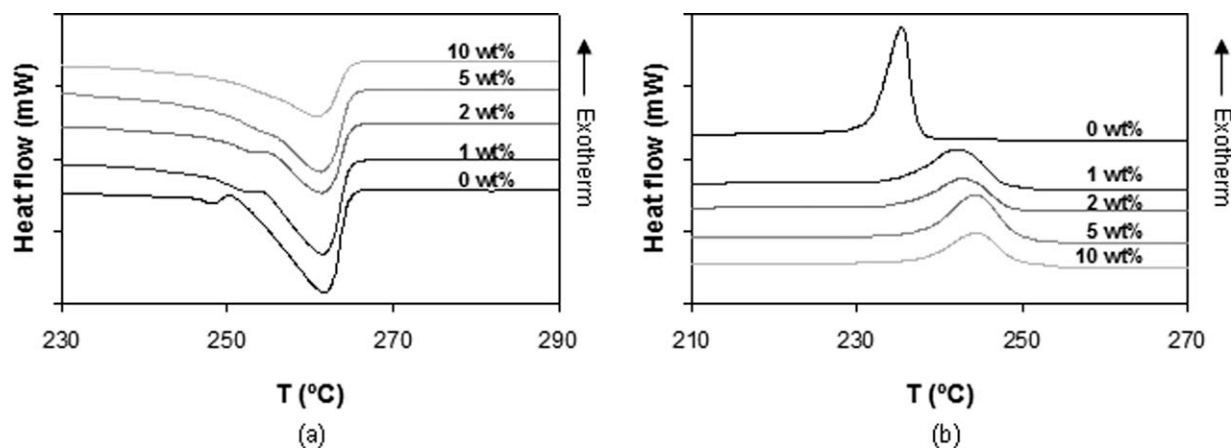|	Solvent processing			*In situ* polymerization			Melt-compounding		
Sample	T_m (°C)	T_c (°C)	X_c (%)	T_m (°C)	T_c (°C)	X_c (%)	T_m (°C)	T_c (°C)	X_c (%)
PA66	261	235	36.7	258	230	32.8	261	235	38.6
PA66/CNF-p	262	241	38.4	254	231	33.3	262	243	37.8

Figure 9 DSC thermograms for solvent-processed composites at various CNF-p concentrations from (a) heating and (b) cooling cycles.

The texture of the NH_3 [Fig. 5(c)] and EDA [Fig. 5(d)] samples prepared by *in situ* polymerization also appears improved over the pristine CNFs, indicative of improved compatibility, dispersion, and distribution. Carboxylated CNFs did not improve dispersion with respect to pristine CNFs [Fig. 5(a,b)]. These results are in agreement with Haggenmueler et al.,[9] who observed better dispersion in amine-functionalized SWCNT/PA66 composites produced by *in situ* polymerization.

As was previously observed with pristine CNFs, the melt-compounded samples yielded the poorest dispersion, with large agglomerates irrespective of surface treatment (Fig. 6). The high viscosity of the melt may impede polymer from breaking apart the CNF nests. On the other hand, CNFs treated in liquid phase form highly compacted granules after drying. These granules become agglomerates in the nanocomposites avoiding in a bigger extend the polymer introduction.[25]

Figure 7 shows histograms of the PA66 nanocomposites containing treated CNFs for solvent and *in situ* processed samples. The sharper peaks found with aminofunctionalized CNFs in both processing methods and their location in the center of the distribution curve prove the better dispersion respect to the nanocomposites with carboxylated CNFs. Ozone functionalization yielded the worst dispersion and distribution, for both solvent and *in situ* samples, as the curves deviate from a normal distribution. It is clear that there are no large agglomerates, but from the chemical point of view, the acidic and carboxylic surface resulted in a bad CNF-matrix affinity. Solvent-processed CNF-HNO_3 presented a distorted curve corroborating earlier optical microscopy evidence in which a segregated morphology was observed.

Histograms from aminofunctionalization are more symmetric and smooth than their pristine CNF counterparts indicating improved CNF-matrix com-

patibility. The most respectable dispersions, as indicated by the histograms, were achieved with *in situ* polymerized CNF-NH_3 and CNF-EDA samples.

Thermal properties

DSC scans were performed to study the crystalline behavior of the 1 wt % nanocomposites. Figure 8 shows the resulting thermograms and the associated crystallization parameters are given in Table III. The crystallization peak of neat PA66 is sharper compared to the solvent and melt-processed nanocomposites. Meng et al.,[26] attributed this change to the influence of CNFs in the wholly crystalline domains. Moreover, CNF addition had no influence on melt temperatures (T_m) but clearly raised crystallization temperatures (T_c) for both solvent and melt-compounded samples. The increase in T_c suggests that the CNFs acted as effective heterogeneous nucleating agents.[26] Contrary to these observations, a T_m decrease was noted in the *in situ* polymerized composite, suggesting a possible variation of the polymer structure when CNFs are present. No change in
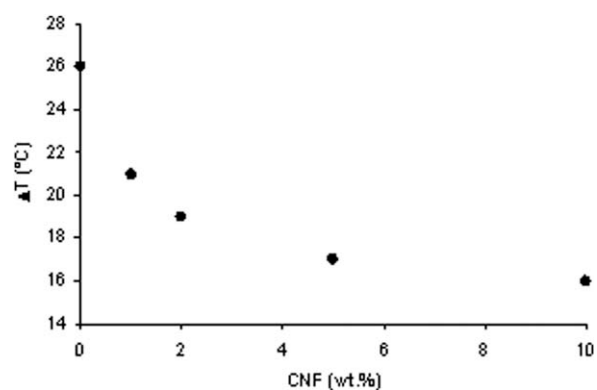

Figure 10 Variation of the degree of supercooling with the CNF content for solvent-processed composites.
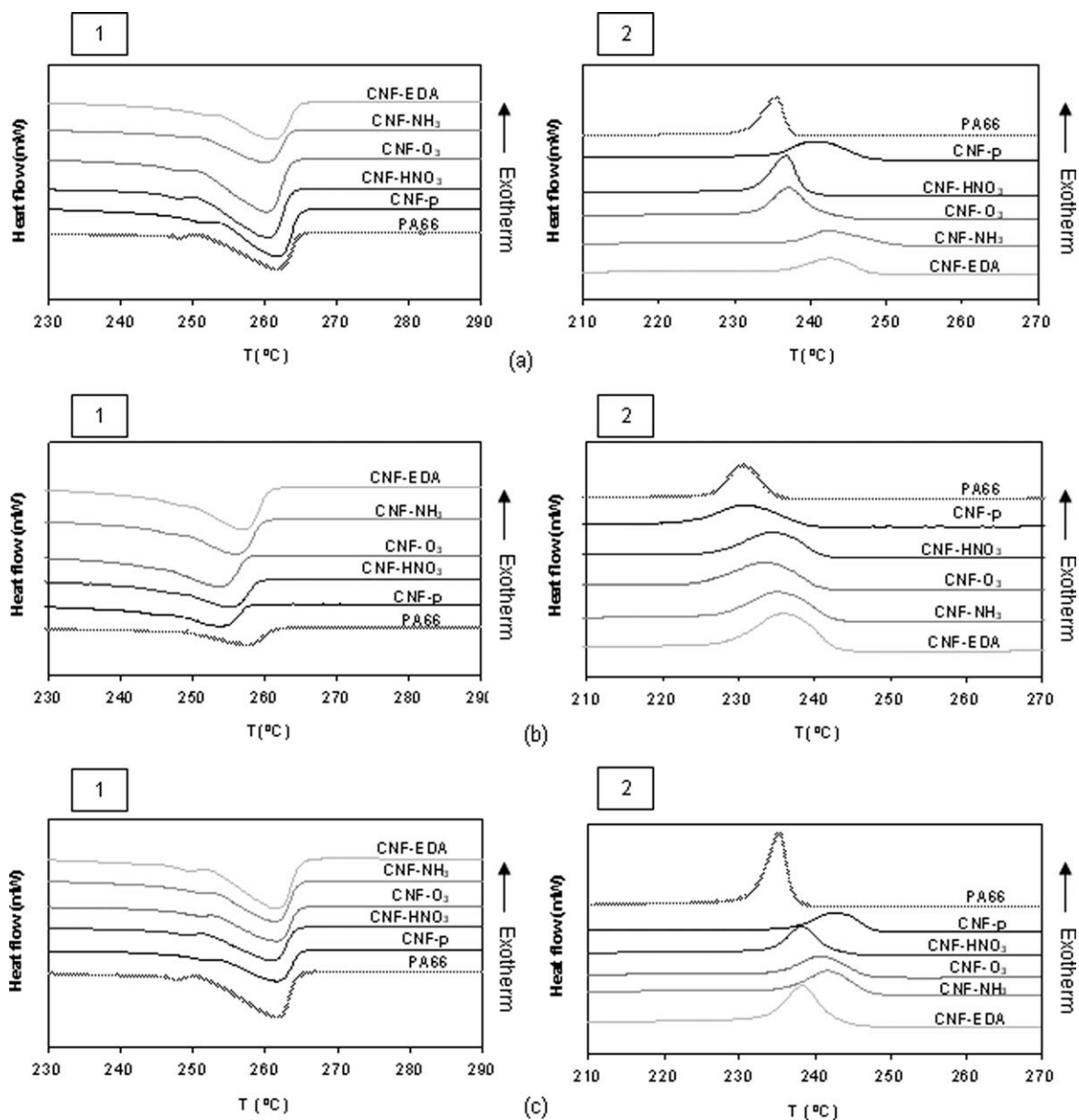
Figure 11 DSC thermograms for (a) solvent-processed, (b) *in situ* polymerized, and (c) melt-compounded nanocomposites at 1 wt % functionalized CNFs from (1) heating and (2) cooling cycles.

T_c was observed as was the case in the composites prepared with the commercially compounded PA66.

The degree of supercooling ($\Delta T = T_m - T_c$) decreases with CNF addition for all the nanocompo-sites, indicating higher nucleation and crystallization rates.[27] These faster crystallization rates are due to the fact that CNFs act as the surface needed for nucleation.

TABLE IV
Crystallization Parameters for Nanocomposites Containing 1 wt % Functionalized CNFs

Sample	Solvent processing			*In situ* polymerization			Melt-compounding		
	T_m (°C)	T_c (°C)	X_c (%)	T_m (°C)	T_c (°C)	X_c (%)	T_m (°C)	T_c (°C)	X_c (%)
CNF-p	262	241	38.4	254	231	33.3	262	243	37.8
CNF-HNO$_3$	260	237	35.8	255	234	32.7	261	238	39.3
CNF-O$_3$	260	237	38.6	254	233	34.8	261	241	38.5
CNF-NH$_3$	260	242	38.5	256	236	34.8	261	242	39.4
CNF-EDA	260	243	54.8	257	236	34.8	262	238	38.0

TABLE V
Variation of the Degree of Supercooling with CNF Functionalization

Sample	ΔT (°C)		
	Solvent processing	*In situ* polymerization	Melt-compounding
CNF-p	21	23	19
CNF-HNO$_3$	23	21	23
CNF-O$_3$	23	21	20
CNF-NH$_3$	18	20	19
CNF-EDA	17	21	24

DSC scans shown in Figure 9 correspond to solvent-processed nanocomposites at various pristine CNF concentrations. Little influence on melt temperature is observed while T_c increases by about 10°C due to the greater number of nucleation sites provided by the CNFs. The increase is apparent at 1 wt % and does not significantly change up to the highest loading (10 wt %). Figure 10 shows the degree of supercooling decrease with CNF addition up to 5 wt %. Larger amount of CNFs hinders the dispersion and agglomerate formation results in a lower increase of the crystallization rate. Papapgeorgiu et al.,[28] observed that nucleation was not affected after 7.5 wt % of nano-SiO$_2$ content because of the tendency of the filler to form aggregates.

To further study the effect of functionalization, DSC scans were performed on 1 wt % nanocomposites from each treatment and processing method (Fig. 11 and Table IV). Figure 11(a), corresponding to the solvent-processed nanocomposites, and Table IV, show that both T_c and X_c present variations when compared to the pristine CNFs. While T_c remained unchanged in nanocomposites with nitrogen-functionalized CNFs, it clearly decreased in both oxygen-functionalized CNF samples, which also exhibited the poorest dispersion. More obvious is the X_c increase in CNF-EDA, unseen in the CNF-

NH$_3$ sample. Nanofiber aspect ratio in the CNF-EDA sample is believed to be lower than that of both pristine and CNF-NH$_3$ due to the prior nitric acid treatment and polymer chain mobility is less likely to be restricted by the lower aspect ratio nanofibers. But strong surface interaction of CNF-EDA with the matrix makes up for the low aspect ratio. This interaction results in the confinement and restriction of the movement of the polymer molecules, reducing the degree of supercooling and increasing the X_c (Table V). Sengupta et al.,[8] reported similar observations about aspect ratio and interfacial interaction in their PA66/MWCNT composites.

Thermograms from the *in situ* polymerized samples are shown in Figure 11(b). The most noteworthy difference with respect to the pristine CNF nanocomposite is an increase in T_c, especially for the nitrogen treatments. This change does not occur in solvent or melt-processed samples implying that the functional groups present on the surface of the nanofibers may have reacted with the matrix during polymerization. Crystallization rate increase might be associated to the reaction and the subsequent enhanced CNF-matrix interaction (Table V).

Regarding melt-compounded materials [Fig. 11(c)], a decrease in T_c and the crystallization rates agrees with the initial hypothesis that CNFs treated in the liquid phase become easily agglomerated and compacted before processing. Thus, it is more difficult for polymer chains to access individual nanofibers and nucleation sites are suppressed.

Electrical properties

The effect of processing method on surface resistivity is shown in Figure 12(a). Melt-compounded nanocomposites appeared insulators even at high CNF loadings. The large agglomerates observed in the micrographs of Figure 2 prevented conductive
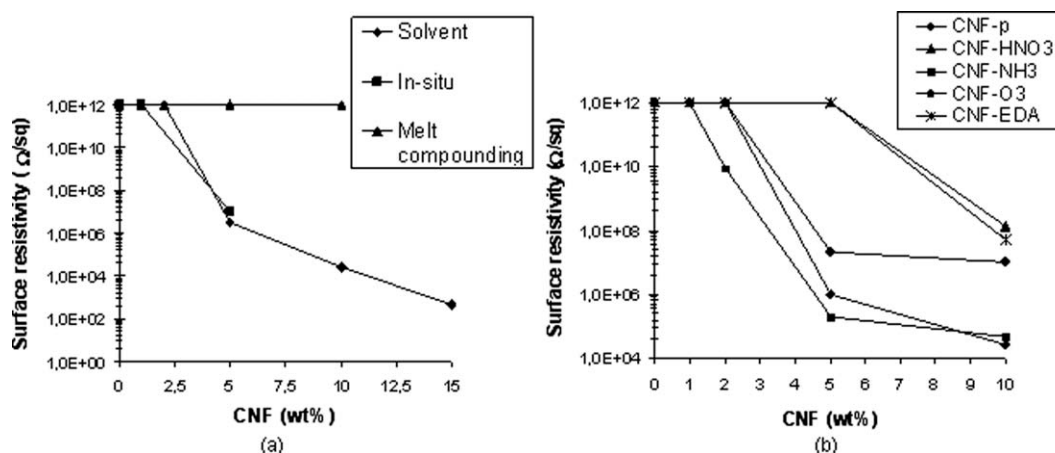

Figure 12 Percolation curves for (a) PA66/GANF by different processing methods and (b) functionalized CNF by solvent processing.

network formation. Percolation is achieved in both solvent and *in situ* processed composites between 2.5 and 5 wt %. Well dispersed but poorly distributed reinforcement oftentimes promotes percolative network formation.[29] Percolation threshold also depends heavily on nanofiber aspect ratio. Longer CNFs are more likely to form percolative networks and at lower volume fractions.[30] The melt-compounding process tends to result in more nanofiber shortening than both the solvent and *in situ* methods thus delaying network formation.

Figure 12(b) compares surface resistivities for solvent-processed nanocomposites with pristine and the various treated CNFs. Percolation was attained at high loadings (between 5 and 10 wt %) for CNF-HNO_3 and CNF-EDA due to nitric acid-induced nanofiber shortening. Network formation was achieved at much lower loadings for CNF-NH_3 and CNF-O_3 (1–5 wt %).

Subsequent to percolation, CNF-O_3 did not reach resistivity values similar to the CNF and CNF-NH_3 samples. O_3 treatments result in some nanofiber damage through the introduction of surface defects and a loss of aromaticity that reduces nanofiber conductivity. As noted in "Dispersion" section, nitrogen-containing groups in the CNF-NH_3 sample appeared to increase CNF-matrix interaction. This led to a slightly lower percolation threshold than the pristine CNFs.

CONCLUSIONS

Processing method profoundly influences CNF dispersion. Samples obtained by the solvent method exhibited the best dispersion, followed by *in situ* polymerization, while melt-compounded nanocomposites offered nonuniform distribution and contained large agglomerates. CNF functionalization is also influential on dispersion. Broadly comparing the treatments, the most homogeneous nanofiber dispersion and distributions were achieved by incorporating nitrogen groups rather than carboxylic groups due to the stronger interaction between the matrix and basic groups. Moreover, treatment with nitric acid and ozonization contributed to nanofiber segregation between amorphous and crystalline zones of the PA66, hindering dispersion.

Electrical conductivity and percolation threshold are dependent on processing method. Large agglomerates in the melt-compounded samples prevented network formation. Solvent processing and *in situ* polymerization led to better dispersions, which positively influenced electrical conductivity. Aspect ratio plays an important role in conductivity. Larger aspect ratio CNFs promote percolative network formation at lower volume fractions. Regarding CNF functionalization, liquid treatments resulted in nanofiber damage, reducing aspect ratio ultimately leading to higher percolation

thresholds. Gas phase treatments preserved nanofiber structure and morphology resulting in lower percolation thresholds. Finally, the amine-containing surface groups of the CNF-NH_3 sample led to enhanced matrix interactions, shown by an increase in T_c. This effect makes the ammonia-treated nanofibers to exhibit the best electrical performance.

References

1. Sengupta, R.; Sabharwal, S.; Bhowmick, A. K.; Chaki, T. K. Polym Degrad Stab 2006, 91, 1311.
2. Sahoo, N. G.; Cheng, H. K. F.; Cai, J.; Li, L.; Chan, S. H.; Zhao, J.; Yu, S. Mater Chem Phys 2009, 117, 313.
3. Moniruzzaman, M.; Winey, K. I. Macromolecules 2006, 39, 5194.
4. Lawrence, J. G.; Berhan, L. M.; Nadarajah, A. ACS Nano 2008, 2, 1230.
5. Breuer, O.; Sundararaj, U. Polym Compos 2004, 25, 630.
6. Ajayan, P. M.; Tour, J. M. Nature 2007, 447, 1066.
7. Ramanathan, T.; Liu, H.; Brinson, L. C. J Polym Sci B: Polym Phys 2004, 43, 2269.
8. Sengupta, R.; Ganguly, A.; Sabharwal, S.; Chaki, T. K.; Bhowmick, A. K. J Mater Sci 2007, 42, 923.
9. Haggenmueller, R.; Du, F.; Fischer, J. E.; Winey, K. I. Polymer 2006, 47, 2381.
10. Krause, B.; Pötschke, P.; Häußler, L. Compos Sci Technol 2009, 69, 1505.
11. Krause, B.; Ritschel, M.; Tãschner, C.; Oswald, S.; Gruner, W.; Leonhardt, A.; Pãtschke, P. Compos Sci Technol 2010, 70, 151.
12. Linares, A.; Canalda, J. C.; Cagiao, M. E.; Ezquerra, T. A. Compos Sci Technol 2011, 71, 1348.
13. Martin-Gullon, I.; Vera, J.; Conesa, J. A.; Gonzalez, J. L.; Merino, C. Carbon 2006, 44, 1572.
14. Palmeri, M. J.; Putz, K. W.; Brinson, L. C. ACS Nano 2010, 4, 4256.
15. Lakshminarayanan, P. V.; Toghiani, H.; Pittman C. U. Jr. Carbon 2004, 42, 2433.
16. Sham, M.-L.; Kim, J.-K. Carbon 2006, 44, 768.
17. Jansen, R. J. J.; van Bekkum, H. Carbon 1994, 32, 1507.
18. Ramanathan, T.; Fisher, F. T.; Ruoff, R. S.; Brinson, L. C. Chem Mater 2005, 17, 1290.
19. Boehm, H. P. in Advances in Catalysis; Eley, D. D., Pines, H. and Weisz, P. B., Eds.; Academic Press, Heidelberg, Germany, 1966, p 179–274.
20. Lozano, K.; Bonilla-Rios, J.; Barrera, E. V. J Appl Polym Sci 2001, 80, 1162.
21. Morales-Teyssier, O.; Sãnchez-Valdes, S.; Ramos-de Volle, L. F. Macromol Mater Eng 2006, 291, 1547.
22. Campoy, I.; Gómez, M. A.; Marco, C. Polymer 1998, 39, 6279.
23. Chavarria, F.; Paul, D. R. Polymer 2004, 45, 8501.
24. Xi, Y.; Yamanaka, A.; Bin, Y.; Matsuo, M. J Appl Polym Sci 2007, 105, 2868.
25. Li, J.; Fang, Z.; Tong, L.; Gu, A.; Liu, F. J Appl Polym Sci 2007, 106, 2898.
26. Meng, H.; Sui, G. X.; Fang, P. F.; Yang, R. Polymer 2008, 49, 610.
27. Szymczyk, A.; Roslaniec, Z.; Zenker, M.; García-Gutiérrez, M. C.; Hernández, J. J.; Rueda, D. R.; Nogales, A.; Ezquerra, T. A. Exp Polym Lett 2011, 5, 977.
28. Papageorgiou, G. Z.; Achilias, D. S.; Bikiaris, D. N.; Karayannidis, G. P. Thermochim Acta 2005, 427, 117.
29. Al-Saleh, M. H.; Sundararaj, U. Carbon 2009, 47, 2.
30. Balberg, I.; Anderson, C. H.; Alexander, S.; Wagner, N. Phys Rev B 1984, 30, 3933.